

## **Thermal cycling induced evolution and colossal exchange bias in MnPS<sub>3</sub>/Fe<sub>3</sub>GeTe<sub>2</sub> van der Waals heterostructures**

Aravind Puthirath Balan<sup>1‡\*</sup>, Aditya Kumar<sup>1‡</sup>, Patrick Reiser<sup>3</sup>, Joseph Vas<sup>4</sup>, Thibaud Denneulin<sup>4</sup>, Khoa Dang Lee<sup>9</sup>, Tom G Saunderson<sup>1,10</sup>, Märta Tschudin<sup>3</sup>, Clement Pellet-Mary<sup>3</sup>, Debarghya Dutta<sup>3</sup>, Carolin Schrader<sup>3</sup>, Tanja Scholz<sup>5</sup>, Jaco Geuchies<sup>7</sup>, Shuai Fu<sup>7</sup>, Hai Wang<sup>7</sup>, Alberta Bonanni<sup>6</sup>, Bettina V. Lotsch<sup>5</sup>, Ulrich Nowak<sup>8</sup>, Gerhard Jakob<sup>1</sup>, Jacob Gayles<sup>9</sup>, Andras Kovacs<sup>4</sup>, Rafal E. Dunin-Borkowski<sup>4</sup>, Patrick Maletinsky<sup>3\*</sup>, Mathias Kläui<sup>1,2\*</sup>

<sup>1</sup>Institute of Physics, Johannes Gutenberg University Mainz, Staudinger Weg 7, 55128 Mainz, Germany.

<sup>2</sup>Centre for Quantum Spintronics, Department of Physics, Norwegian University of Science and Technology, 7491 Trondheim, Norway.

<sup>3</sup>Department of Physics, University of Basel, Klingelbergstrasse 82, Basel CH-4056, Switzerland

<sup>4</sup>Ernst Ruska-Centre for Microscopy and Spectroscopy with Electrons and Peter Grünberg Institute, Forschungszentrum Jülich, 52425 Jülich, Germany

<sup>5</sup>Max Planck Institute for Solid State Research, Heisenbergstraße 1, 70569 Stuttgart, Germany

<sup>6</sup>Institute of Semiconductor & Solid-State Physics, Johannes Kepler University Linz, Altenberger Straße 69, 4040 Linz, Austria

<sup>7</sup>Max Planck Institute for Polymer Research Mainz, Ackermannweg 10, 55128 Mainz, Germany

<sup>8</sup>Department of Physics, University of Konstanz, Universitaetsstrasse 10, 78464 Konstanz, Germany

<sup>9</sup>Department of Physics, University of South Florida, Tampa, FL 33620, USA.

<sup>10</sup>Peter Grünberg Institut and Institute for Advanced Simulation, Forschungszentrum Jülich and JARA, Jülich, 52425, Germany.

10, 78464 Konstanz, Germany

‡These authors contributed equally

\*Correspondence to : [aravindputhirath@uni-mainz.de](mailto:aravindputhirath@uni-mainz.de),  
[patrick.maletinsky@unibas.ch](mailto:patrick.maletinsky@unibas.ch), [klaeui@uni-mainz.de](mailto:klaeui@uni-mainz.de)

**Keywords:** vdW magnetic materials, exchange bias, vdW heterostructures, manganese thiophosphate,  $\text{Fe}_3\text{GeTe}_2$

## **Abstract**

The exchange bias phenomenon, inherent in exchange-coupled ferromagnetic and antiferromagnetic systems, has intrigued researchers for decades. Van der Waals materials, with their layered structure, provide an optimal platform for probing such physical phenomena. However, achieving a facile and effective means to manipulate exchange bias in pristine van der Waals heterostructures remains challenging. In this study, we investigate the origin of exchange bias in  $\text{MnPS}_3/\text{Fe}_3\text{GeTe}_2$  van der Waals heterostructures. Our work demonstrates a method to modulate unidirectional exchange anisotropy, achieving an unprecedented nearly 1000% variation through simple thermal cycling. Despite the compensated interfacial spin configuration of  $\text{MnPS}_3$ , magneto-transport measurements reveal a huge 170 mT exchange bias at 5 K, the largest observed in pristine van der Waals antiferromagnet-ferromagnet interfaces. This substantial magnitude of the exchange bias is linked to an anomalous weak ferromagnetic ordering in  $\text{MnPS}_3$  below 40 K. On the other hand, the tunability of exchange bias during thermal cycling is ascribed to the modified arrangement of interfacial atoms and changes in the vdW gap during field cooling. Our findings highlight a robust and easily adjustable exchange bias in van der Waals antiferromagnetic/ferromagnetic heterostructures, presenting a straightforward approach to enhance other interface related spintronic phenomena for practical applications.

## **Introduction**

Exchange bias (EB) is a unidirectional anisotropy that occurs in exchange-coupled antiferromagnetic/ferromagnetic (AFM/FM) systems, such as thin films and core-shell nanostructures.<sup>[1-3]</sup> While this phenomenon has been studied in thin-film heterostructures for

over four decades, a comprehensive theoretical understanding remains a challenge for condensed matter physics community. It is now well established, that there is not just one specific origin of the exchange bias phenomenon. Instead, several theoretical models of EB in magnetic systems have been developed, considering various possible spin configurations at the interface, including in-plane (IP) collinear, perpendicular, and out-of-plane (OOP) arrangements.<sup>[3]</sup> Furthermore, EB has been studied in polycrystalline AFM/FM interfaces, and the phenomenological aspects are extensively discussed by O’Grady *et al.*<sup>[4]</sup> However, most theoretical models that successfully describe EB consider the AFM/FM interfaces to be well-defined without any roughness or grain boundaries.<sup>[2,5-7]</sup> In contrast, only a few theories tackle defective AFM/FM interfaces and how they contribute to EB.<sup>[8-10]</sup> The discovery of van der Waals (vdW) magnetic materials provides a unique solution to this issue by providing an extensive library of FM and AFM vdW materials.<sup>[11]</sup> Their intrinsic layered nature and ability to form heterostructures offer a convenient way to obtain defect-free and atomically flat single-crystalline AFM/FM interfaces, which has sparked renewed interest in the investigation of EB in vdW heterostructures.<sup>[12]</sup>

Although vdW AFM/FM heterostructures offer potentially ideal interfaces for EB, their weaker exchange coupling hinders their suitability for storage applications because of the presence of the vdW gap.<sup>[13]</sup> Recent efforts have focused on extrinsic control of exchange coupling by manipulating the AFM/FM interface registry, involving methods like applying pressure and laser irradiation.<sup>[14-15]</sup> Recent successful experiments have demonstrated significant EB in vdW heterostructures through coverage control and the application of gate voltage.<sup>[16-17]</sup> Additionally, the introduction of an oxide layer has shown promise, albeit challenges in controllability and repeatability.<sup>[18,19]</sup> Despite these advances, a straightforward and efficient strategy to precisely tune EB in vdW heterostructures remains elusive. Such a

strategy is crucial for enabling diverse applications that require tailored EB strengths, such as magnetic recording and data storage.

Here, to understand the interplay between interface structure, magnetic order, and exchange bias, we extensively investigate MnPS<sub>3</sub>/Fe<sub>3</sub>GeTe<sub>2</sub> AFM/FM vdW heterostructures in a multimodal approach, combining magneto-transport anomalous Hall effect, superconducting quantum interference device (SQUID) magnetometry, scanning nitrogen-vacancy center magnetometry (S-NVM) and scanning transmission electron microscopy (STEM). Despite featuring a fully compensated AFM/FM interface<sup>[20-22]</sup>, the vdW MnPS<sub>3</sub>/Fe<sub>3</sub>GeTe<sub>2</sub> system exhibits a remarkably high interfacial exchange-coupling strength. This gives rise to a significant EB, the most substantial observed in untreated van der Waals AFM/FM interfaces so far. Notably, the strength of interfacial coupling can be modulated through thermal cycling. This thermal manipulation results in a decisive alteration in the magnitude of EB, exceeding 1000%. This thermal cycling can be implemented concurrently with the field-cooling procedure used to establish EB, thus eliminating the need for any additional steps. The unprecedented and significant alteration in EB magnitude through straightforward thermal cycling may set a platform for manipulating various other interface-related spintronic phenomena in vdW heterostructures. The subsequent section summarizes and discusses the extensive EB observed in the MnPS<sub>3</sub>/Fe<sub>3</sub>GeTe<sub>2</sub> system, elucidating its origin and the evolution induced by thermal cycling.

## **Results and Discussion**

To fabricate the device, we transfer a MnPS<sub>3</sub>/Fe<sub>3</sub>GeTe<sub>2</sub> heterostructure onto prefabricated Au/Cr (25 nm/5 nm) Hall contacts deposited on a Si/SiO<sub>2</sub> (300 nm) substrate. We employ a Polydimethylsiloxane (PDMS) and polymethylmethacrylate (PMMA) assisted dry transfer method inside an inert atmosphere-maintained glovebox to transfer and stack flakes of

Fe<sub>3</sub>GeTe<sub>2</sub> and MnPS<sub>3</sub> in the specified order. This results in the formation of a MnPS<sub>3</sub>/Fe<sub>3</sub>GeTe<sub>2</sub> vdW heterostructure with a clean interface (refer to **Figure 1c** inset). To minimise the risk of oxidation due to brief exposure of the heterostructure to air during wire-bonding of the voltage and current pads for anomalous Hall measurements, we cap the obtained heterostructure with a hexagonal boron nitride (h-BN) flake. Additionally, unless otherwise stated, special care is taken to limit the air exposure time to below 30 minutes in all the devices measured during this investigation. For a detailed sample preparation procedure, please refer to the methods section. The wire-bonded device is loaded into a high-field cryostat, and anomalous Hall effect measurements are conducted using magneto-transport techniques.

To induce EB, the device consisting of h-BN-capped MnPS<sub>3</sub>/Fe<sub>3</sub>GeTe<sub>2</sub> vdW heterostructure is subjected to a field-cooling process starting from 120 K (a temperature above the Neel temperature of MnPS<sub>3</sub>, which is 78 K) down to the desired temperature ( $T = 5$  K) with an OOP magnetic field of +8 T & -8 T. After reaching the desired temperature, the magnetic field is ramped down to zero, and the anomalous Hall voltage ( $V_{xy}$ ) measured by sweeping the field in the OOP direction. The normalized anomalous Hall voltage ( $V_{xy}$ ) is used to plot the hysteresis (refer to **Figure 1a**). The EB field ( $H_{EB}$ ) is determined using the formula  $H_{EB} = \frac{(H_C^+ + H_C^-)}{2}$  where  $H_C^+$  and  $H_C^-$  represent the positive and negative switching fields. Surprisingly, a large negative  $H_{EB}$  of magnitude 170 mT is observed at 5 K. This observation is unexpected, considering the previously claimed fully compensated magnetic order of MnPS<sub>3</sub>.<sup>[21-22]</sup> Continuing our investigation, we measure the trend of  $H_{EB}$  as a function of increasing temperature by executing a similar procedure at various temperatures, ranging from 5 K to 80 K (refer to **Figure 1b**).  $H_{EB}$  is calculated for each measurement and plotted against the temperature, as illustrated in **Figure 1c**. It is evident that  $H_{EB}$  is at a maximum (170 mT) at 5 K and gradually decreases with increasing temperature, disappearing at 40 K—well below the Néel temperature ( $T_N$ ) of MnPS<sub>3</sub> (78 K). The presence of such a large EB that disappears at a

temperature much lower than the  $T_N$  indicates that the compensated antiferromagnetic order of MnPS<sub>3</sub> cannot solely explain the observed EB.

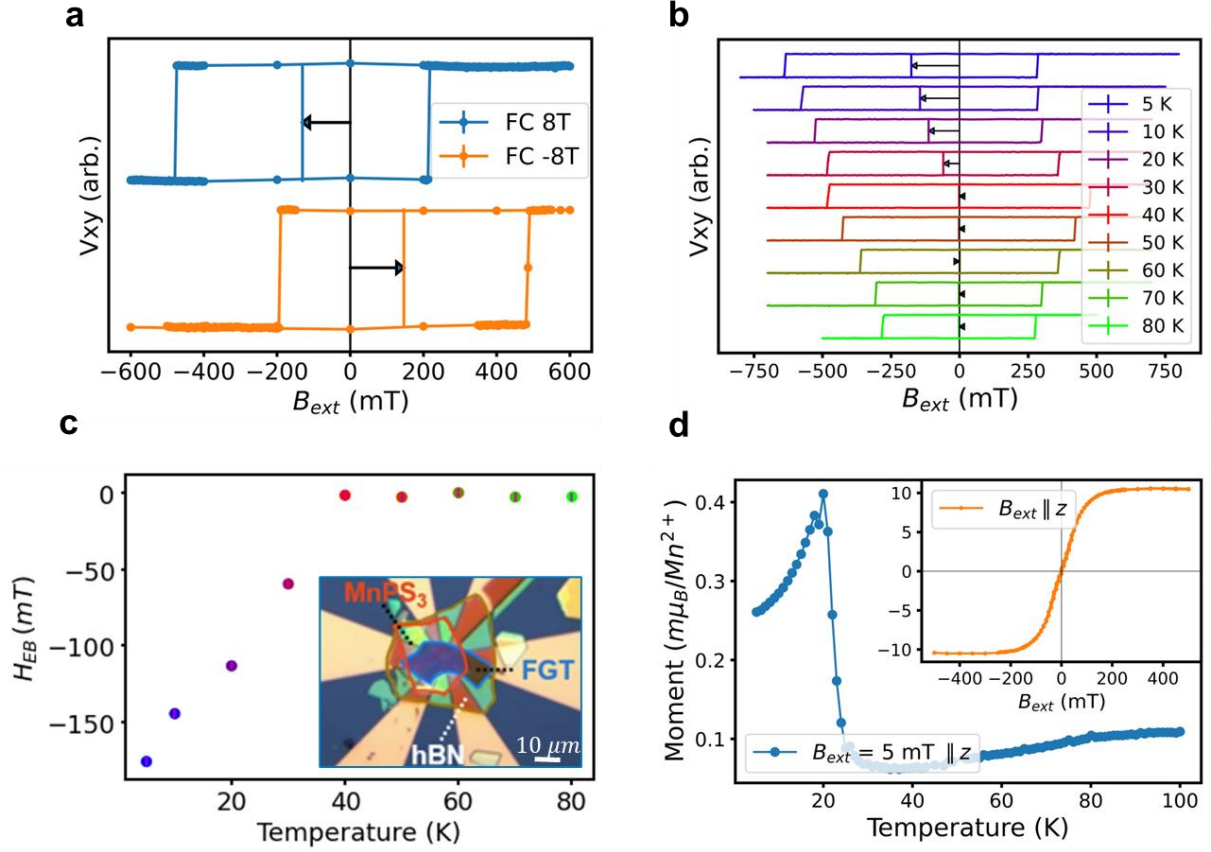


**Figure 1.** **a)** Anomalous Hall voltage ( $V_{xy}$ ) as a function of the magnetic field after  $\pm 8$  T field-cooling process measured at 5 K, **b)**  $V_{xy}$  as a function of magnetic field after +8 T field-cooling and measured at temperatures ranging from 5 K to 80 K. **c)** The  $H_{EB}$  vs.  $T$  plot, derived from the data presented in *Figure 1b*, reveals the blocking temperature of MnPS<sub>3</sub> to be approximately 40 K. The inset provides an optical image of the measured van der Waals heterostructure. **d)** Magnetization ( $M$ ) vs. Temperature ( $T$ ) curve measured for the bulk MnPS<sub>3</sub> crystal in an OOP orientation. The inset displays an isothermal  $M$  vs.  $H$  curve at 5 K.

To understand more about the origin of EB, we employ dc SQUID magnetometry to obtain magnetization versus temperature ( $M$  vs.  $T$ ) and magnetization versus magnetic field ( $M$  vs.  $H$ ) plot at 5 K for a bulk MnPS<sub>3</sub> crystal while maintaining the magnetic field orientation OOP. The results are depicted in **Figure 1d**. Below 40 K, an anomalous magnetic moment is

observed, as indicated by the onset in the magnetic moment. The onset of this anomalous moment correlates with the onset of the nonzero  $H_{EB}$  (refer to **Figure 1c**). A clear saturation in  $M$  vs.  $H$  hysteresis at 5 K with finite coercivity is presented as further supporting evidence (see **Figure 2d** inset).

To investigate the nature and anisotropy of the anomalous ferromagnetic moment in MnPS<sub>3</sub> flakes, we next utilize S-NVM. To probe the static magnetic state of a few-layer MnPS<sub>3</sub> of comparable thickness to the Fe<sub>3</sub>GeTe<sub>2</sub>/MnPS<sub>3</sub> heterostructure under investigation, S-NVM is performed on isolated MnPS<sub>3</sub> flakes at 4.5 K. The nitrogen-vacancy (NV) center can be scanned across the sample to record the emanating stray magnetic field. This enables the inference of the underlying magnetization, with a typical spatial resolution of 30-100 nm (**Figure 2a** and details in the methods section). The examined sample comprises two isolated MnPS<sub>3</sub> flakes capped by an h-BN flake (see **Figure 2a**).

We find that a clear stray magnetic field arises from the edge of the MnPS<sub>3</sub> flake, indicating an uncompensated magnetic moment that deviates from its expected compensated antiferromagnetic order (see **Figure 2b**). A linecut is taken across the flake edge with an applied field of 150 mT along the NV axis and a magnetic model of a homogeneous magnetization is fitted to the stray field. The best agreement between the model and the data is found for Mn magnetic moments pointing along the IP direction parallel to the NV center projection to the sample plane. A magnetization of  $M = 2170 (\pm 40) \text{ m}\mu_B/\text{nm}^2$  is obtained corresponding to a bulk magnetization of  $15.8 (\pm 0.3) \text{ m}\mu_B/\text{Mn}$  for the flake thickness of  $57.5 (\pm 4.5) \text{ nm}$  obtained by the simultaneously recorded topography (refer to **Figure 2c**). Using these parameters, the stray field of the flake is simulated, and a good qualitative agreement between data and simulation indeed confirms the easy plane anisotropy of the Mn moments. This finding is in good agreement with the recent report that suggests MnPS<sub>3</sub> undergoes a spin-reorientation transition, characterized by Mn moments that goes from an OOP Heisenberg-type collinear antiferromagnetic order to the IP XY type order.<sup>[23]</sup> A larger magnetization (see Figure

2d) is observed for the magnetic hysteresis ( $M$  vs.  $H$ ) measured with the sweeping field oriented IP with respect to the bulk  $\text{MnPS}_3$  crystal as compared to that when the sweeping field is oriented OOP, which provides further supporting evidence for the IP anisotropy.

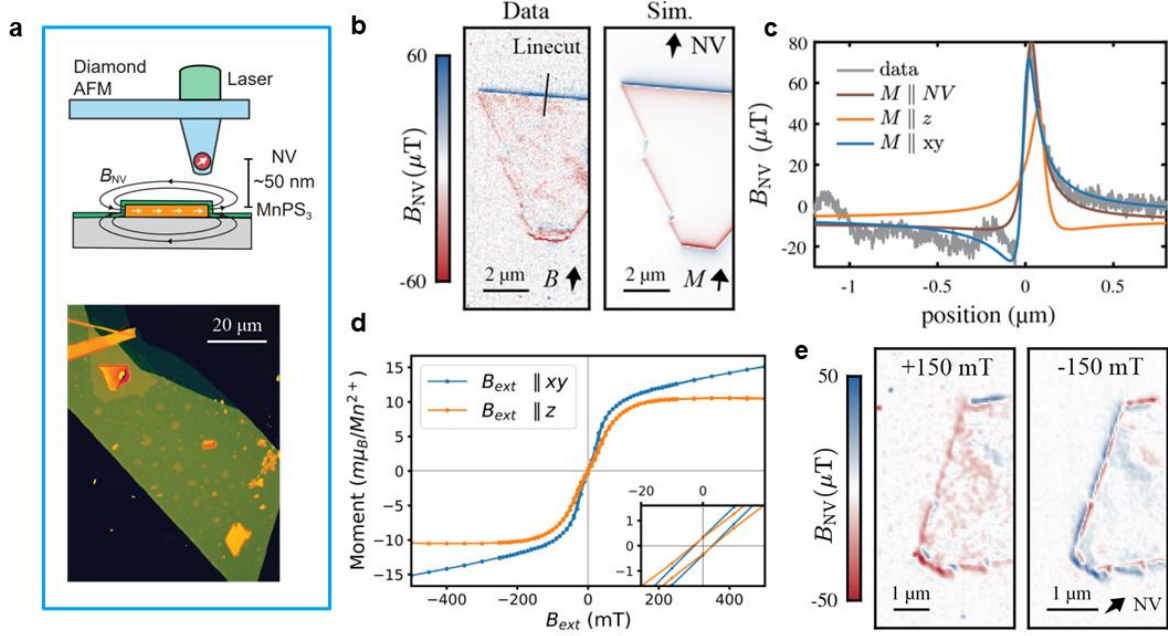


**Figure 2.** **a)** Schematics of S-NVM setup: A NV center is brought into contact with the surface, and the stray magnetic field of the sample is recorded by performing an ODMR measurement at each pixel with the microscope image of the studied sample underneath. It comprises two  $\text{MnPS}_3$  flakes of  $\sim 50\text{nm}$  height capped by h-BN. **b)** Stray magnetic field image of the flake recorded at  $B_{ext} = 150\text{ mT}$  applied along the NV axis as indicated by the arrows. Simulation of the stray magnetic field assuming IP orientation of the magnetization. **c)** Linecut taken across the edge of the flake as indicated by the line. Different magnetization models are used to fit the data. The best agreement is found with the IP orientation of the flake. **d)** DC SQUID magnetometry data of a bulk crystal taken at 5 K. Though bulk  $\text{MnPS}_3$  is reported to be an ideal Heisenberg AFM, a finite magnetic moment with remanence is observed, suggesting a transition in spin-ordering at low temperatures. **e)** Stray magnetic field image for opposite field polarities. Reversing field polarity between  $+150\text{ mT}$  and  $-150\text{ mT}$  yields opposite polarity of the stray field, indicating a switchable weak ferromagnetic ordering.



In agreement with the measurements on the bulk crystal, at lower fields, the uncompensated moment shows a linear field dependence of  $(\partial M/\partial B_{ext}) = 92 (\pm 9) m \frac{\mu_B}{\text{Mn}}/\text{T}$  (refer to **Figure S1** in *Supporting information*) with a finite remanent magnetic moment of  $1.5 (\pm 0.7) m\mu_B/\text{Mn}$  close to zero-field. Importantly, the remanent moment maintains the magnetization direction unchanged at lower fields even after reversing the polarity, as evident from identical red contrast observed in images acquired at  $\pm 5$  mT (refer to **Figure S2** in *Supporting information*). It is apparent from the S-NVM measurements that the remanent moment can potentially be bound to the AFM state of MnPS<sub>3</sub> and persists even above the maximum applied field of  $\mp 500$  mT (maximum field reachable by the used vector magnet) along the NV direction. However, the stray fields measured at  $\pm 150$  mT, as indicated in **Figure 2e**, exhibit an inverted contrast. This observation suggests that few-layer MnPS<sub>3</sub> flakes possess a larger switchable magnetic moment (below  $\pm 150$  mT). This magnetic moment displays a linear variation with the applied field and predominates over the discernible remanent moment bound to the AFM state of MnPS<sub>3</sub>, thereby contributing to the finite coercivity (refer to **Figure S1** in *Supporting information*).

Albeit of a soft magnetic nature, the field required to switch the uncompensated moment of the MnPS<sub>3</sub> flake is greater than 5 mT, whereas the bulk crystal has a coercive field of less than 5 mT (refer to **Figure 2d inset**). This contrasting behavior between bulk crystal and an exfoliated flake could be attributed to confinement effects.<sup>[20]</sup> Nevertheless, the few-layer MnPS<sub>3</sub> flake exhibits a remanent magnetic moment bound to the AFM state of MnPS<sub>3</sub>. This distinctive magnetic moment serves as a pinning source, thus possibly explaining the observed EB in the Fe<sub>3</sub>GeTe<sub>2</sub>/MnPS<sub>3</sub> heterostructures.

The findings from bulk SQUID magnetometry and high resolution and high sensitivity S-NVM measurements unequivocally establish the presence of net uncompensated magnetic moment in MnPS<sub>3</sub>. The observed EB can be ascribed to the pinning of Fe<sub>3</sub>GeTe<sub>2</sub> by the intrinsic

weak anomalous magnetic moment associated with the AFM state in MnPS<sub>3</sub> flakes at temperatures below 40 K. This phenomenon arises due to a low-temperature spin-reorientation transition from OOP Heisenberg-type order to IP XY-type order.<sup>[23]</sup> The emergence of a robust EB resulting from a low-temperature compensated antiferromagnetic (AFM) to weak ferromagnetic (FM) transition has not been previously documented in vdW heterostructures. This observation has repercussions that could enable spintronic phenomena in MnPS<sub>3</sub> and other similar vdW systems, where such transitions can occur.

Having established the origin of EB, we next study the evolution of the  $H_{EB}$  strength. We find that the observed  $H_{EB}$  at a specific temperature undergoes a substantial variation, characterized by a dynamic evolution across successive iterations while maintaining experimental conditions unchanged. We conduct 15 consecutive anomalous Hall voltage measurements at 5 K while implementing an 8 T field-cooling from 120 K for an h-BN-capped MnPS<sub>3</sub>/Fe<sub>3</sub>GeTe<sub>2</sub> device (Device 1). We determine  $H_{EB}$  for each measurement. Surprisingly, despite maintaining identical experimental conditions, we observe different values of  $H_{EB}$  after every heating and field-cooling cycle. To assess the universality of this observed metamorphosis, we fabricate two additional h-BN-capped MnPS<sub>3</sub>/Fe<sub>3</sub>GeTe<sub>2</sub> devices (Device 2 and Device 3) and follow a similar measurement protocol to obtain  $H_{EB}$  for 15 consecutive field-cooling measurements (see **Figure S3** in *Supporting information*). All three devices consistently demonstrate that a free-standing vdW AFM-FM interface is dynamic under thermal cycling, strongly influencing interface-related phenomena, particularly EB. The details of the evolving EB observed for 15 consecutive field-cooling measurements at 5 K for this device are summarized in *Supplementary Figure S3*. In general, the expression for  $H_{EB}$  for an exchange biased AFM/FM system is given by the modified Meiklejohn–Bean model, equation (1),<sup>[24]</sup>

$$H_{EB} = \frac{J_{EB}}{\mu_0 M_{FM} t_{FM}} \quad (1)$$

where,  $J_{EB}$  is the interfacial exchange coupling energy,  $M_{FM}$  is the saturation magnetization of the FM, and  $t_{FM}$  is the thickness of ferromagnetic layer. Now, the thermal cycling induced evolution of EB can only be influenced by the parameter of the numerator  $J_{EB}$  while the denominator remains unchanged since the materials remain unaltered. However, the numerator  $J_{EB}$ , which is directly related to the interface characteristics can be dependent on the intercrystalline distance ( $\xi$ ). Here, in the case of a vdW AFM/FM heterostructure, the interfacial ferromagnetic layer consists of exchange-coupled interfacial AFM and FM layers separated by a vdW gap. Huang *et. al.* measured EB in FM/AFM vdW heterostructure and showed that EB decreases with increase in interlayer distance.<sup>[15]</sup> This implies that a thermal cycling assisted vdW gap modification can be a potential reason for the evolution of EB.

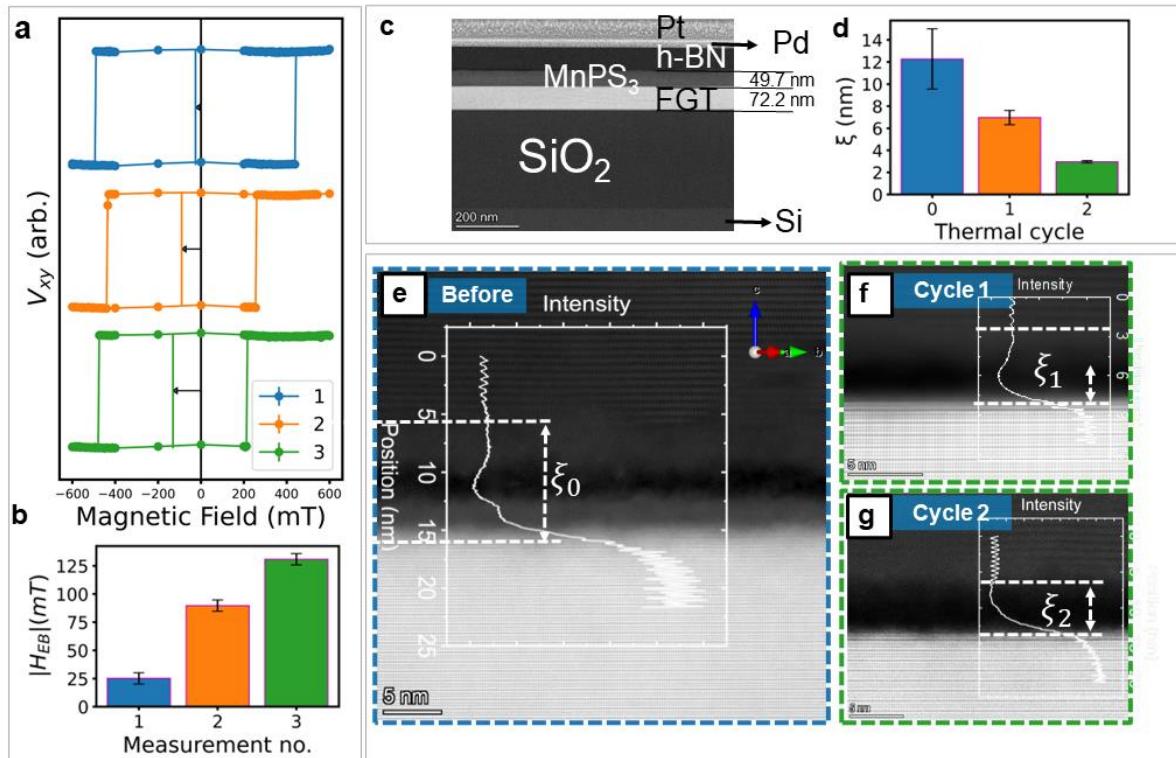


**Figure 3.** Evolution of EB due to change in van der Waal gap caused by heating-cooling cycles. **a)** AHE hysteresis loops measured after different heating-cooling cycles. **b)** The magnitude of EB varies between 25 mT and 132 mT. More measurements on additional samples can be found in the Supporting

information. **c)** Low magnification cross-sectional HAADF-STEM image of the  $\text{Fe}_3\text{GeTe}_2/\text{MnPS}_3/\text{h-BN}$  vdW heterostructure. **d)** A histogram summarising the observed modification of intercrystalline distances ( $\xi$ ) measured in the images (e, f, g) at room temperature before (e) and after two consecutive cooling and heating cycles (f & g), **e)** a high-resolution HAADF-STEM image of the sample, and  $\xi_0$  is the intercrystalline distance measured at room temperature. The measurements were repeated two more times after cooling-heating cycles **f)** and **g)**, and  $\xi_1$  &  $\xi_2$  are the corresponding intercrystalline distances measured. The intercrystalline distances measured after each cycle ( $\xi_1$  &  $\xi_2$ ) differed from the initial value ( $\xi_0$ ).

By examining  $H_{EB}$  obtained during 15 consecutive cycles for device 1 (**Figure 3a & 3b**), we can see that the value of  $H_{EB}$  varies between a minimum of  $25 (\pm 5)$  mT and a maximum of  $132 (\pm 5)$  mT which corresponds to an enhancement of  $> 500 \%$  in magnitude. This is even greater ( $\sim 1000 \%$ ) in device 2 (D2) and device 3 (D3) (refer to **Figure S3** in *Supporting information*). Such a huge enhancement in  $H_{EB}$  by merely thermal cycling is unprecedented and calls for further understanding of the underlying mechanism. For that, we construct a heterostructure with an h-BN-capped  $\text{MnPS}_3/\text{Fe}_3\text{GeTe}_2$  configuration on a  $\text{Si}/\text{SiO}_2$  (300 nm) substrate, and we perform cross-sectional STEM measurements during two consecutive cooling-heating cycles. The findings are presented in **Figure 3c-g**. The low-resolution high-angle annular dark-field STEM (HAADF-STEM) image of the h-BN/ $\text{MnPS}_3/\text{Fe}_3\text{GeTe}_2$  cross-section is provided in **Figure 3c**. High-resolution STEM imaging of the vdW  $\text{MnPS}_3/\text{Fe}_3\text{GeTe}_2$  heterostructure interface is conducted at room temperature. We obtain  $\xi_0 \cong 12 (\pm 3)$  nm (see **Figure 3e**) which we define as the initial thickness of exchange coupled interfacial FM layer equal to the distance between crystalline region (inter-crystalline distance) of  $\text{MnPS}_3$  and  $\text{Fe}_3\text{GeTe}_2$ . It is evident from the HRSTEM image that  $\xi$  is constituted of the vdW gap and an amorphous region formed by intermigration of atoms between  $\text{MnPS}_3$  and  $\text{Fe}_3\text{GeTe}_2$  as evident from the STEM-EDX elemental mapping (refer to **Figure S7** in *Supporting information*). Subsequently, we reevaluate the interface twice at room temperature,

each time on a freshly prepared lamella following the ex-situ cooling of the heterostructure to liquid nitrogen temperature and subsequent warming to room temperature (for experimental details, please refer to the respective methods section). Remarkably,  $\xi$  undergoes significant modification, as evident from the corresponding cross-sectional STEM images (see **Figure 3f** & **3g**). The values obtained for  $\xi$  after two thermal cycles are  $\xi_1 \cong 7 (\pm 1)$  and  $\xi_2 \cong 3 (\pm 0.03)$  nm, respectively, and are summarised in the bar graph (**Figure 3d**). We observe a reduction of approximately  $9 (\pm 3)$  nm in  $\xi$  after two consecutive thermal cycles, scaling equivalently to the enhancement in the magnitude of  $H_{EB}$  in one of the measured devices (Device 1). We additionally investigated how the vdW gap influences the total energy of the system in MnPS<sub>3</sub>/Fe<sub>3</sub>GeTe<sub>2</sub> heterostructure from first principles (refer to **Figure S8**). Our findings imply an absolute hard limit on the minimal vdW gap of 6 Å, whilst also showing that the difference between the total energy for the distances that go beyond this limit is very small. This means that the system is stable for finite vdW gaps beyond the hard limit and can relax into metastable states with varying vdW gaps without much energy cost. The origin of such a significant variation in the inter-crystalline distance and the modified vdW gap can be attributed to the thermal expansion coefficient mismatch induced strain<sup>[25]</sup> between Fe<sub>3</sub>GeTe<sub>2</sub> and MnPS<sub>3</sub>, which would be significant at the interface. This straightforward and efficient approach for customizing vdW gaps can be expanded to influence other spintronic phenomena related to interfaces<sup>[26]</sup> within vdW heterostructures. However, the magnetic nature of the amorphous layers formed due to the intermigration of atoms across the vdW gap and how it contributes to the observed evolving EB is still unresolved, and we consider this would be an interesting future direction of study that goes beyond the scope of the current work.

## Conclusion

In conclusion, we observed a huge EB in MnPS<sub>3</sub>/Fe<sub>3</sub>GeTe<sub>2</sub> vdW heterostructures despite MnPS<sub>3</sub> having a compensated collinear antiferromagnetic spin structure below the Néel

temperature of 78 K. Notably, our experiments reveal that significant exchange bias appears only below 40 K, a phenomenon attributed to an inherent anomalous weak ferromagnetic moment emerging in MnPS<sub>3</sub>. This phenomenon has remained largely unexplored thus far, and it originates from a small fraction of spins transitioning from an OOP Heisenberg-type order to an IP XY-type order. The magnitude of EB is found to exhibit an evolving nature that leads to a variation of  $H_{EB}$  up to 1000 % achievable merely by thermal cycling. This evolving nature of EB observed is due to the modified interfacial registry of the vdW AFM/FM heterostructure characterized by a modified thickness of the exchange-coupled interfacial FM layer, as confirmed by cross-sectional STEM measurements. The observed remarkable EB in vdW AFM/FM heterostructures, subject to tunability through straightforward thermal cycling-induced vdW gap engineering reveals significant potential for the facile manipulation of EB in vdW heterostructures for magnetic storage and sensor applications. This simple strategy can be implemented for tuning other phenomena at interfaces within van der Waals heterostructures.

## Methods

*MnPS<sub>3</sub>/Fe<sub>3</sub>GeTe<sub>2</sub> vdW heterostructure fabrication:* Bulk ‘single crystals’ of MnPS<sub>3</sub> and Fe<sub>3</sub>GeTe<sub>2</sub> were obtained from our collaborators in Johannes Kepler University Linz and Max Planck Institute for Solid State Research Stuttgart, respectively. The bulk crystals were subjected to Raman spectroscopy measurements, and the obtained spectra agree well with the standard Raman modes expected for MnPS<sub>3</sub><sup>[27]</sup> and Fe<sub>3</sub>GeTe<sub>2</sub><sup>[28]</sup> (refer to **Figure S4** in *Supporting information*). The bulk crystals were exfoliated down to a few layered flakes onto a Si/SiO<sub>2</sub> (300 nm) substrate inside a glovebox, with the O<sub>2</sub> and H<sub>2</sub>O levels maintained well below 0.5 ppm. A suitable few layered flakes of both Fe<sub>3</sub>GeTe<sub>2</sub> and MnPS<sub>3</sub> were selected using an optical microscope. We employ a Polydimethylsiloxane (PDMS) and polymethylmethacrylate (PMMA) assisted dry transfer method inside the glovebox to transfer and stack multi-layered flakes of Fe<sub>3</sub>GeTe<sub>2</sub> and MnPS<sub>3</sub> in the specified order. This results in

the formation of an MnPS<sub>3</sub>/Fe<sub>3</sub>GeTe<sub>2</sub> vdW heterostructure with a clean interface. To minimise the risk of oxidation due to brief exposure of the heterostructure to air during wire-bonding of the voltage and current pads for anomalous Hall measurements, we cap the obtained heterostructure with an h-BN flake. Additionally, special care is taken to limit the air exposure time to below 30 minutes in all the devices measured before loading onto the high field cryostat sample space, where a low-pressure helium environment is maintained during this investigation unless otherwise stated. Atomic Force Microscopy is carried out to measure the thickness of MnPS<sub>3</sub> and Fe<sub>3</sub>GeTe<sub>2</sub> flakes of the heterostructures (refer to **Figure S5** in *Supporting information*).

*Magneto-transport measurements:* The h-BN-capped MnPS<sub>3</sub>/Fe<sub>3</sub>GeTe<sub>2</sub> heterostructures were then wire-bonded and immediately loaded onto a variable temperature insert (VTI) cryostat in which we can apply a magnetic field up to 12 T for anomalous Hall effect (AHE) measurements. Since MnPS<sub>3</sub> is an insulating antiferromagnet, the current will only flow through the metallic Fe<sub>3</sub>GeTe<sub>2</sub> layer. The cross-sectional area of the current channel along an 80 nm × 5 μm Fe<sub>3</sub>GeTe<sub>2</sub> flake (Device 1) is  $4 \times 10^{-13} \text{ m}^2$ , and is used to calculate the current density, which is approximately  $2.5 \times 10^6 \text{ Am}^{-2}$  for an applied current of 1 μA. A 1 μA current is transmitted through the Fe<sub>3</sub>GeTe<sub>2</sub> flake along the  $x$ -direction and the anomalous Hall voltage ( $V_{xy}$ ) is measured across the transverse terminals along the  $y$ -direction. The field is always applied in the OOP orientation for the field-cooling process and the field sweeping. A Keithley 2400 source meter is used to flow current through the device, and a Keithley 2182a nanovoltmeter is used to measure voltage.

*DC SQUID Magnetometry Measurements:* Magnetic hysteresis loops ( $M$  vs.  $H$ ) and temperature-dependent magnetization curves ( $M$  vs.  $T$ ) were acquired for a bulk MnPS<sub>3</sub> crystal using a Quantum Design SQUID MPMS3 Magnetometer. The  $M$  vs.  $H$  measurements involved sweeping the magnetic field in both IP and OOP orientations relative to the crystal's bulk

structure. Meanwhile,  $M$  vs.  $T$  measurements were conducted over a temperature range of 5 K to 100 K, applying a magnetic field of 50 Oe in an OOP orientation.

*Scanning nitrogen-vacancy center magnetometry (S-NVM) measurements:* S-NVM is a potent, non-invasive imaging technique suitable for probing weak magnetic fields on the order of  $\mu\text{T}$  with a spatial resolution of (30-100 nm), especially suitable for the investigation of magnetism in vdW nanomagnets.<sup>[29–31]</sup> An all-diamond atomic force tip containing a single NV near the apex of the tip ( $\approx 10\text{-}20$  nm) is brought close to the sample's surface.<sup>[32]</sup> The NV center hosts an optically addressable spin that is initialized and read out all optically while it is coherently manipulated by externally applied microwaves. The upper spin levels show a Zeeman effect, which allows for a precise measurement of the stray magnetic field along the NV quantization axis.<sup>[33]</sup> S-NVM measurements are performed in a commercial cryogenic atomic force microscopy system (AttoCube, AttoLiquid 1000) with a home-built NV magnetometry setup (details in Ref<sup>[34]</sup>). For AFM operation, the NV tip is mounted on a quartz capillary glued to a quartz tuning fork. The tuning fork is operated in shear mode with amplitude feedback to keep the tip at a constant height above the surface. The tip is positioned by Piezo positioners and scanners, providing a scan range of  $15\ \mu\text{m} \times 15\ \mu\text{m}$ . The complete atomic force microscopy setup is placed in a sample chamber at 100 mbar He atmosphere located in the liquid bath cryostat at a base temperature of 4.3 K. A 0.5 T vector magnet is used to apply an external magnetic field. The emission of a 532 nm laser (Laser Quantum GEM) is collimated on a 0.81 NA objective (AttoCube LT-APO) and subsequently focused on the NV. The resulting photoluminescence (PL) is collected via the excitation path and separated by a dichroic mirror (Thorlabs DMLP567). The PL photons are collected by an avalanche photodiode (Excelitas SPCM-AQRH-33). The microwave signal for coherent manipulation of the NV spin is produced by a signal generator (SRS SG384) and an IQ modulator (Polyphase Microwave AM0350A), amplified (Minicircuit ZHL-42W+), and transmitted by a bondwire  $\sim 100$  nm close to the NV tip. An arbitrary waveform generator (Spectrum instrumentation DN2.663-4) is used



to pulse the microwave driving and the laser emission. The resonance frequency of the spin transition is recorded at each pixel to determine the corresponding stray magnetic field from the Zeeman induced frequency shift. The NV is excited with a 500  $\mu\text{s}$  laser pulse, which initializes the NV into the  $m_s = 0$  spin state. Next, a near resonant microwave  $\pi$  pulse is applied to the NV center. The resulting spin state is read out by a second 500  $\mu\text{s}$  laser pulse that also reinitializes the spin state for the following pulse cycle. Two different measurement schemes are used: a) full optical detected magnetic resonance spectra are recorded at each pixel, and b) a feedback protocol is used to track the resonance frequency of the NV. While the first scheme requires more integration time but is less prone to measurement artifacts, the second scheme provides higher field sensitivity, resulting in a lower noise level. S-NVM is carried out at a base temperature of 4.5 K, with an external bias field of 150 mT applied along the determined NV axis before the measurements. The NV axis of the tip used for this work was measured to be  $56^\circ (\pm 2^\circ)$  with the OOP direction. This pre-application of an external bias field aims to optimize sensor performance at low temperatures.<sup>[35]</sup>

*Scanning transmission electron microscopy (STEM) Measurements:* The STEM imaging is done using a double corrected TFS Spectra 300 microscope operated in STEM mode at 300 kV. The microscope is equipped with a high-brightness X-FEG, monochromated source and a piezo CompuStage, and can achieve sub-Ångström resolution. The transmission electron microscopy (TEM) lamella is tilted, so the  $\text{Fe}_3\text{GeTe}_2$  is in the  $\langle 0001 \rangle$  zone axis. A high-angle annular dark-field (HAADF) detector is used to image the interface between the  $\text{Fe}_3\text{GeTe}_2$  and  $\text{MnPS}_3$ . The intercrystalline distance between the  $\text{Fe}_3\text{GeTe}_2$  and  $\text{MnPS}_3$  stacks responsible for the exchange coupling is measured using high resolution STEM. The required TEM lamella is prepared using the focused ion beam (FIB) technique. The lamella is prepared by cutting a stack of  $\text{Fe}_3\text{GeTe}_2/\text{MnPS}_3$  on a (300 nm)  $\text{SiO}_2/\text{Si}$  wafer and encapsulated in h-BN using a FEI make Helios 460F dual beam FIB-SEM. A 5 nm thick Pd layer is deposited on top of the stack to prevent charging. Two protective layers of electron beam deposited Pt and ion beam Carbon

were deposited atop the area of interest to reduce the sample contamination due to gallium implantation. A TEM lamella with an electron transparent window of  $\sim 50$  nm thickness is cut from the chip, and the distance between the  $\text{Fe}_3\text{GeTe}_2$  and  $\text{MnPS}_3$  layers is measured (see **Figure S6** in *Supporting information* for a summary of stepwise STEM cross-section lamella fabrication). To study the change in the inter-crystalline distance with cooling cycles, it is preferred to cool down the entire crystal rather than the TEM lamella since the process of lamella fabrication reduces the sample conditions due to the strains introduced due to the production of thin TEM lamella and Ga implantation. The  $\text{SiO}_2/\text{Si}$  chip consisting of the vdW heterostructure is cooled down to 77 K by dropping the chip into  $\text{LN}_2$  in a dewar and waiting at least 8 hours until all the  $\text{LN}_2$  evaporated. After the chip warms up to room temperature, it is dried using an  $\text{N}_2$  gun to remove any moisture condensing on the surface. Additional TEM lamellae were prepared after each cooling cycle to measure the inter-crystalline distance. Energy dispersive X-ray (EDX) spectroscopy is carried out using an FEI Titan TEM equipped with a Schottky field emission gun operated at 200 kV, a CEOS probe aberration corrector, a high angle annular dark-field detector (HAADF) and a Super-X EDX detection system. Elemental maps and profiles were obtained using the Thermo Scientific Velox software. The results are summarized in **Figure S7** in *Supporting information*.

*First principles calculations:* First principles calculations were performed using the VASP software package <sup>[36-39]</sup>. Distances between 5 and 12 Å were chosen and a full spin-polarized self-consistency with FM and AFM starting ground states chosen for FGT and  $\text{MnPS}_3$  respectively. The calculations were performed using the GGA exchange correlation functional<sup>[40]</sup> and converged on a 8 by 8 k-mesh with an energy cutoff of 270eV. The results are summarized in **Figure S8** in *Supporting information*.

## Acknowledgments

APB and AK contributed equally to this work. We acknowledge funding from Alexander von Humboldt Foundation for Humboldt Postdoctoral Fellowship (Grant number: Ref 3.5-IND-1216986-HFST-P), EU Marie-Curie Postdoctoral Fellowship ExBiaVdW (Grand Id: 101068014), Deutsche Forschungsgemeinschaft (DFG, German Research Foundation) – Spin+X TRR 173–268565370 (Projects No. A01, No. B02 and A12), DFG Project No. 358671374, Graduate School of Excellence Materials Science in Mainz (MAINZ) GSC 266, the MaHoJeRo (DAAD Spintronics network, Projects No. 57334897 and No. 57524834), the Research Council of Norway (Centre for Quantum Spintronics - QuSpin No. 262633), The European Union’s Horizon 2020 Research and Innovation Programme under grant agreement 856538 (project “3D MAGIC”). S.F. acknowledges the China Scholarship Council for financial support.

## References:

- [1] T. Blachowicz, A. Ehrmann, M. Wortmann, *Nanomaterials (Basel)* **2023**, 13.
- [2] W. H. Meiklejohn, C. P. Bean, *Physical Review* **1957**, 105, 904.
- [3] T. Blachowicz, A. Ehrmann, *Coatings* **2021**, 11, 122.
- [4] K. O’Grady, L. E. Fernandez-Outon, G. Vallejo-Fernandez, *Journal of Magnetism and Magnetic Materials* **2010**, 322, 883.
- [5] L. Néel, presented at *Annales de Physique*, **1967**.
- [6] D. Mauri, H. C. Siegmann, P. S. Bagus, E. Kay, *Journal of Applied Physics* **1987**, 62, 3047.
- [7] R. Yanes, J. Jackson, L. Udvardi, L. Szunyogh, U. Nowak, *Physical review letters* **2013**, 111, 217202.
- [8] A. P. Malozemoff, *Physical Review B* **1987**, 35, 3679.
- [9] T. C. Schulthess, W. H. Butler, *Physical Review Letters* **1998**, 81, 4516.
- [10] P. Miltényi, M. Gierlings, J. Keller, B. Beschoten, G. Güntherodt, U. Nowak, & K. D. Usadel, *Physical Review Letters* **2000**, 84, 4224.
- [11] M. Gibertini, M. Koperski, A. F. Morpurgo, K. S. Novoselov, *Nature Nanotechnology* **2019**, 14, 408.
- [12] M.-H. Phan, V. Kalappattil, V. O. Jimenez, Y. Thi Hai Pham, N. W. Y. A. Y. Mudiyansele, D. Detellem, C.-M. Hung, A. Chanda, T. Eggers, *Journal of Alloys and Compounds* **2023**, 937, 168375.
- [13] C. Hu, K. N. Gordon, P. Liu, J. Liu, X. Zhou, P. Hao, D. Narayan, E. Emmanouilidou, H. Sun, Y. Liu, H. Brawer, A. P. Ramirez, L. Ding, H. Cao, Q. Liu, D. Dessau, N. Ni, *Nature Communications* **2020**, 11, 97.
- [14] T. Li, S. Jiang, N. Sivadas, Z. Wang, Y. Xu, D. Weber, J. E. Goldberger, K. Watanabe, T. Taniguchi, C. J. Fennie, K. Fai Mak, J. Shan, *Nature Materials* **2019**, 18, 1303.
- [15] X. Huang, L. Zhang, L. Tong, Z. Li, Z. Peng, R. Lin, W. Shi, K.-H. Xue, H. Dai, H. Cheng, D. de Camargo Branco, J. Xu, J. Han, G. J. Cheng, X. Miao, L. Ye, *Nature Communications* **2023**, 14, 2190.
- [16] Z. Ying, B. Chen, C. Li, B. Wei, Z. Dai, F. Guo, D. Pan, H. Zhang, D. Wu, X. Wang, S. Zhang, F. Fei, F. Song, *Nano Letters* **2023**, 23, 765.
- [17] S. Albarakati, W.-Q. Xie, C. Tan, G. Zheng, M. Algarni, J. Li, J. Partridge, M. J. S. Spencer, L. Farrar, Y. Xiong, M. Tian, X. Wang, Y.-J. Zhao, L. Wang, *Nano Letters* **2022**, 22, 6166.
- [18] T. Zhang, Y. Zhang, M. Huang, B. Li, Y. Sun, Z. Qu, X. Duan, C. Jiang, S. Yang, *Advanced Science* **2022**, 9, 2105483.

- [19] A. P. Balan, A. Kumar, T. Scholz, Z. Lin, A. Shahee, S. Fu, T. Denneulin, A. Kovacs, R. E. Dunin-Borkowski, H. I. Wang, *arXiv preprint arXiv:2303.13167* **2023**.
- [20] C. Tan, J. Lee, S.-G. Jung, T. Park, S. Albarakati, J. Partridge, M. R. Field, D. G. McCulloch, L. Wang, C. Lee, *Nature Communications* **2018**, 9, 1554.
- [21] P. A. Joy, S. Vasudevan, *Physical Review B* **1992**, 46, 5425.
- [22] G. Long, H. Henck, M. Gibertini, D. Dumcenco, Z. Wang, T. Taniguchi, K. Watanabe, E. Giannini, A. F. Morpurgo, *Nano Letters* **2020**, 20, 2452.
- [23] S. Chaudhuri, C. N. Kuo, Y. S. Chen, C. S. Lue, J. G. Lin, *Physical Review B* **2022**, 106, 094416.
- [24] J. Dubowik, I. Gościańska, *Acta Physica Polonica A* **2015**, 127, 147.
- [25] L. Zhang, H. Wang, X. Zong, Y. Zhou, T. Wang, L. Wang, X. Chen, *Nature Communications* **2022**, 13, 3996.
- [26] F. Hellman, A. Hoffmann, Y. Tserkovnyak, G. S. D. Beach, E. E. Fullerton, C. Leighton, A. H. MacDonald, D. C. Ralph, D. A. Arena, H. A. Dürr, P. Fischer, J. Grollier, J. P. Heremans, T. Jungwirth, A. V. Kimel, B. Koopmans, I. N. Krivorotov, S. J. May, A. K. Petford-Long, J. M. Rondinelli, N. Samarth, I. K. Schuller, A. N. Slavin, M. D. Stiles, O. Tchernyshyov, A. Thiaville, B. L. Zink, *Reviews of Modern Physics* **2017**, 89, 025006.
- [27] Y.-J. Sun, Q.-H. Tan, X.-L. Liu, Y.-F. Gao, J. Zhang, *The Journal of Physical Chemistry Letters* **2019**, 10, 3087.
- [28] X. Kong, T. Berlijn, L. Liang, *Advanced Electronic Materials* **2021**, 7, 2001159.
- [29] L. Thiel, Z. Wang, M. A. Tschudin, D. Rohner, I. Gutiérrez-Lezama, N. Ubrig, M. Gibertini, E. Giannini, A. F. Morpurgo, P. Maletinsky, *Science* **2019**, 364, 973.
- [30] T. Song, Q.-C. Sun, E. Anderson, C. Wang, J. Qian, T. Taniguchi, K. Watanabe, M. A. McGuire, R. Stöhr, D. Xiao, T. Cao, J. Wrachtrup, X. Xu, *Science* **2021**, 374, 1140.
- [31] A. Laraoui, K. Ambal, *Applied Physics Letters* **2022**, 121.
- [32] P. Appel, E. Neu, M. Ganzhorn, A. Barfuss, M. Batzer, M. Gratz, A. Tschöpe, P. Maletinsky, *Review of Scientific Instruments* **2016**, 87.
- [33] L. Rondin, J. P. Tetienne, T. Hingant, J. F. Roch, P. Maletinsky, V. Jacques, *Reports on Progress in Physics* **2014**, 77, 056503.
- [34] L. Thiel, D. Rohner, M. Ganzhorn, P. Appel, E. Neu, B. Müller, R. Kleiner, D. Koelle, P. Maletinsky, *Nature Nanotechnology* **2016**, 11, 677.
- [35] J. Happacher, D. A. Broadway, J. Bocquel, P. Reiser, A. Jimenéz, M. A. Tschudin, L. Thiel, D. Rohner, M. I. G. Puigibert, B. Shields, J. R. Maze, V. Jacques, P. Maletinsky, *Physical Review Letters* **2022**, 128, 177401.
- [36] G. Kresse, J. Hafner, *Physical Review B* **1993**, 47, 558.
- [37] G. Kresse, J. Hafner, *Physical Review B* **1994**, 49, 14251.
- [38] G. Kresse and J. Furthmüller, *Computational Materials Science* **1996**, 6, 15.
- [39] G. Kresse and J. Furthmüller, *Physical Review B* **1996**, 54, 11 169.
- [40] John P. Perdew, Kieron Burke, and Matthias Ernzerhof *Physical Review Letters* **1996**, 77, 3865.

## Supporting Information

### Thermal cycling induced evolution and colossal exchange bias in MnPS<sub>3</sub>/Fe<sub>3</sub>GeTe<sub>2</sub> van der Waals heterostructures

Aravind Puthirath Balan<sup>1‡\*</sup>, Aditya Kumar<sup>1‡</sup>, Patrick Reiser<sup>3</sup>, Joseph Vas<sup>4</sup>, Thibaud Denneulin<sup>4</sup>, Khoa Dang Lee<sup>9</sup>, Tom G Saunderson<sup>1,10</sup>, Märta Tschudin<sup>3</sup>, Clement Pellet-Mary<sup>3</sup>, Debarghya Dutta<sup>3</sup>, Carolin Schrader<sup>3</sup>, Tanja Scholz<sup>5</sup>, Jaco Geuchies<sup>7</sup>, Shuai Fu<sup>7</sup>, Hai Wang<sup>7</sup>, Alberta Bonanni<sup>6</sup>, Bettina V. Lotsch<sup>5</sup>, Ulrich Nowak<sup>8</sup>, Gerhard Jakob<sup>1</sup>, Jacob Gayles<sup>9</sup>, Andras Kovacs<sup>4</sup>, Rafal E. Dunin-Borkowski<sup>4</sup>, Patrick Maletinsky<sup>3\*</sup>, Mathias Kläui<sup>1,2\*</sup>

<sup>‡</sup>These authors contributed equally

\* Correspondence to [aravindputhirath@uni-mainz.de](mailto:aravindputhirath@uni-mainz.de), [patrick.maletinsky@unibas.ch](mailto:patrick.maletinsky@unibas.ch), [klaeui@uni-mainz.de](mailto:klaeui@uni-mainz.de)

#### Characteristics of anomalous weak ferromagnetism in exfoliated MnPS<sub>3</sub> flakes

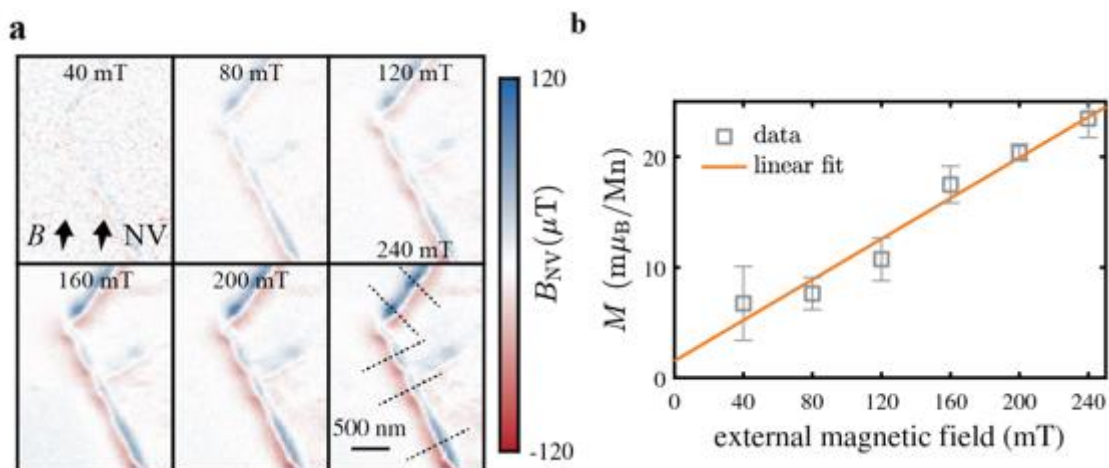


**Figure S1. Field dependence of the uncompensated Moment of MnPS<sub>3</sub>.** **a)** Consecutive images obtained from the isolated MnPS<sub>3</sub> flake at various applied magnetic fields along the NV axis, as indicated by the arrows. The dotted lines in the image acquired at  $B_{ext} = 240$  mT indicate the position for the linecuts used to estimate the signal strength. **b)** Signal strength as estimated from the linecuts shown in **a**. Depicted uncertainties indicate the standard deviation between the linecuts. The axis has been normalized by the magnetization obtained from the linecut shown in Fig. 3. A linear function is fitted through the data points.

**Figure S1** provides a comprehensive analysis of the field dependence of the uncompensated moment of MnPS<sub>3</sub>, shedding light on its magnetic behavior under varying external conditions. Figure S1a presents a series of consecutive images showcasing the isolated MnPS<sub>3</sub> flake under the influence of different applied magnetic fields along the NV axis, as indicated by arrows. Notably, in the image acquired at an external magnetic field strength of  $B_{ext} = 240$  mT, dotted lines demarcate the positions for the subsequent linecuts employed for signal strength estimation. The corresponding results are illustrated in **Figure S1b**. The uncertainties associated with the measurements are denoted by error bars, representing the standard deviation observed between the various linecuts. To provide a normalized perspective, the axis has been scaled by the magnetization acquired from the linecut exhibited in **Figure 3**, ensuring a consistent basis for comparison. Intriguingly, a linear function has been fitted through the data points, offering a mathematical description of the observed relationship between the applied magnetic field and the resulting signal strength.

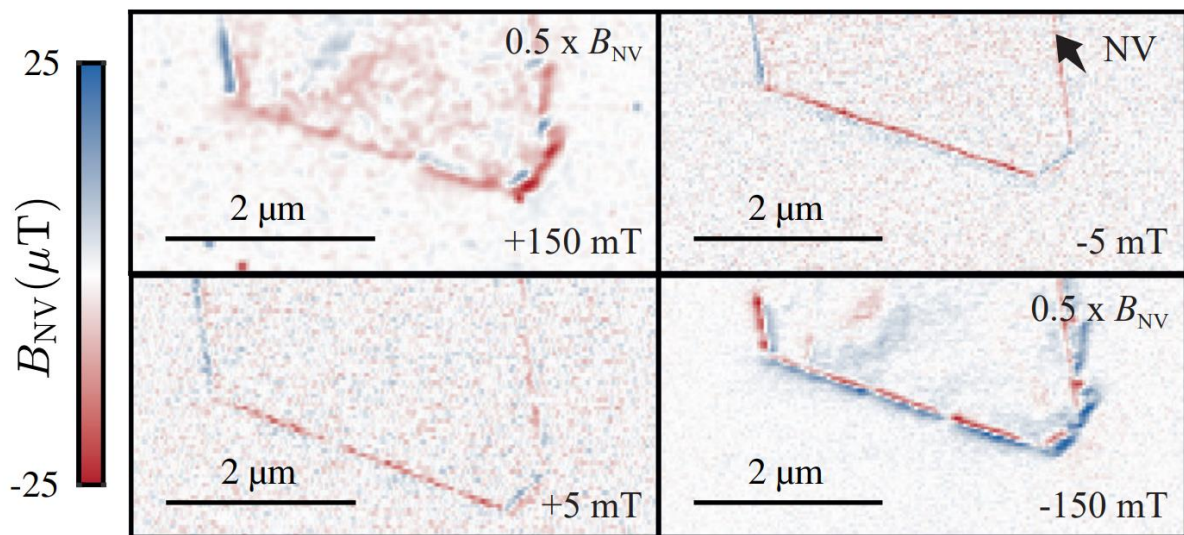


**Figure S2. Hysteresis cycle of the uncompensated moment of MnPS<sub>3</sub> flake.** Consecutive images obtained from the isolated MnPS<sub>3</sub> flake at various applied magnetic fields along the NV axis, as indicated by the arrow. The applied field follows the hysteresis cycle  $B = +150$  mT  $\rightarrow$   $-5$  mT  $\rightarrow$   $-150$  mT  $\rightarrow$   $+5$  mT. Interestingly, though the magnetization switched at

$\pm 150$  mT, the polarity of the remanent magnetization at  $\pm 5$  mT remains unchanged contrary to the SQUID data obtained from a bulk crystal.

**Figure S2** summarizes consecutive images derived from an isolated MnPS<sub>3</sub> flake that were acquired while subjecting it to varying applied magnetic fields along the NV axis, as depicted by the directional arrow. The magnetic field applied to the system followed a hysteresis cycle, specifically transitioning through the values of  $B = +150$  mT,  $-5$  mT,  $-150$  mT, and  $+5$  mT. Notably, an intriguing observation emerged during the analysis, wherein the magnetization exhibited a switch in polarity at magnetic field strengths of  $\pm 150$  mT. However, in stark contrast to the SQUID (Superconducting Quantum Interference Device) data obtained from a bulk crystal, the remanent magnetization at  $\pm 5$  mT retained its polarity, remaining unaltered throughout the cyclic magnetic field perturbation. This unexpected behavior highlights a distinctive aspect of the MnPS<sub>3</sub> flake's magnetic response, deviating from the anticipated trends observed in bulk crystal counterparts. The findings underscore the importance of investigating nanoscale structures for a comprehensive understanding of magnetic properties and their potential implications for applications in nanotechnology and spintronics.

## Thermal cycling induced metamorphosis of exchange bias in $\text{Fe}_3\text{GeTe}_2/\text{MnPS}_3$

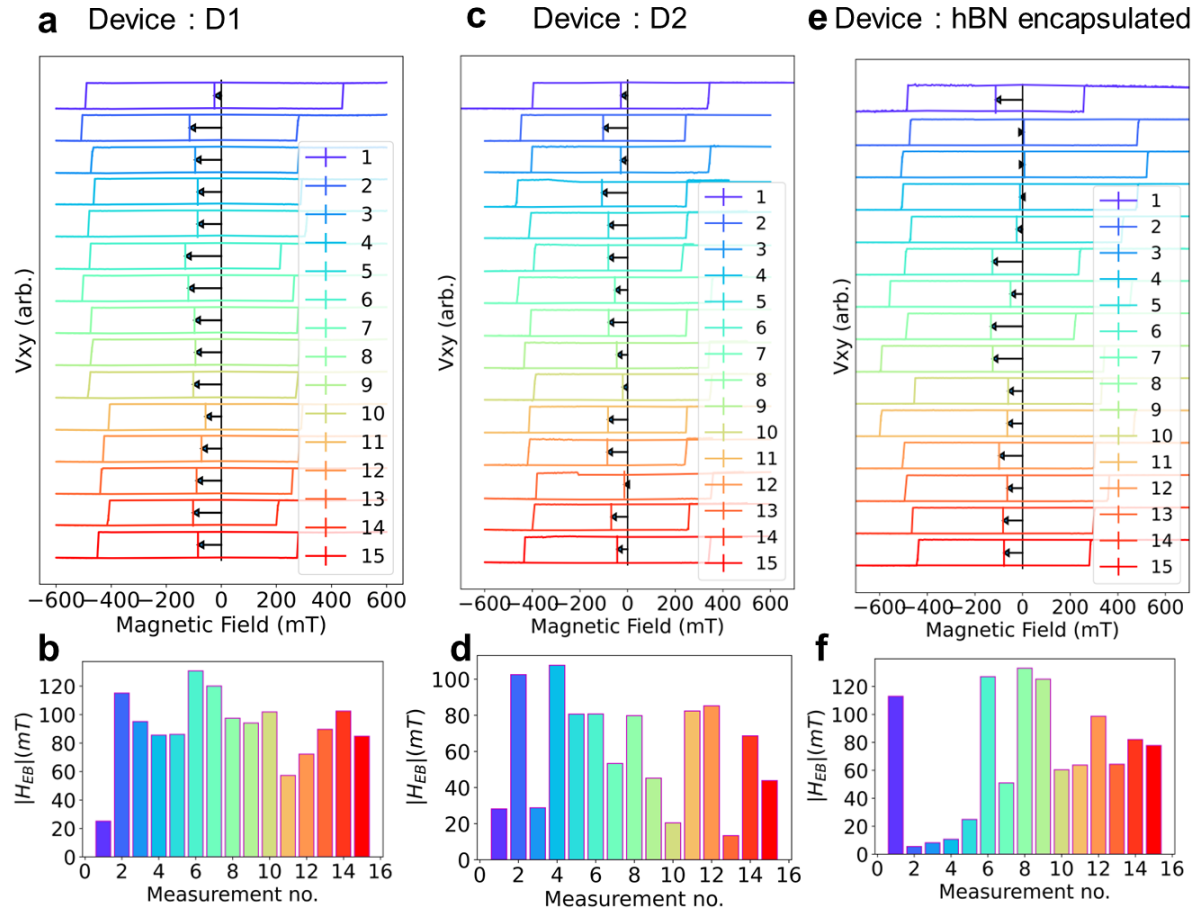


**Figure S3. Thermal cycling induced metamorphosis of exchange bias in  $\text{Fe}_3\text{GeTe}_2/\text{MnPS}_3$  vdW heterostructures.** The top row shows AHE hysteresis plots, and the bottom row summarizes the magnitude of measured exchange bias after each of the 15 consecutive cycles. **a)** and **b)** h-BN/ $\text{MnPS}_3/\text{Fe}_3\text{GeTe}_2$  sample (D1). **c)** and **d)** h-BN/ $\text{MnPS}_3/\text{Fe}_3\text{GeTe}_2$  sample (D2) to confirm reproducibility of evolving exchange bias. **e)** and **f)** h-BN/ $\text{MnPS}_3/\text{Fe}_3\text{GeTe}_2/\text{h-BN}$  sample (D3). This device is fabricated and measured to check the effect of stress from substrate clamping on  $\text{Fe}_3\text{GeTe}_2$  flake due to a mismatch in the thermal expansion coefficient of  $\text{Fe}_3\text{GeTe}_2$  and Si/SiO<sub>2</sub> substrate. However, no significant difference is observed in exchange bias evolution in D3 compared to devices D1 and D2.



**Figure S3** illustrates the dynamic metamorphosis of exchange bias in MnPS<sub>3</sub>/ Fe<sub>3</sub>GeTe<sub>2</sub> van der Waals (vdW) heterostructures induced by thermal cycling. The top row presents anomalous Hall effect (AHE) hysteresis plots, while the bottom row summarizes the measured magnitude of exchange bias after each of the 15 consecutive thermal cycles. The figure is organized into distinct panels, each corresponding to a different heterostructure configuration. **Figures S3a** and **b** showcase the results obtained from the h-BN-capped MnPS<sub>3</sub>/Fe<sub>3</sub>GeTe<sub>2</sub> sample (D1). These panels provide AHE hysteresis plots and document the evolving magnitude of exchange bias across the thermal cycles. Similarly, **Figures 3c and d** present results from a second h-BN capped MnPS<sub>3</sub>/Fe<sub>3</sub>GeTe<sub>2</sub> sample (D2), confirming the reproducibility of the observed evolution in exchange bias.

To investigate the influence of substrate clamping-induced stress on Fe<sub>3</sub>GeTe<sub>2</sub> flake on the dynamic evolution of exchange bias, a device is fabricated with an h-BN encapsulation instead of capping. **Figures 3d and e** depict results obtained for the h-BN encapsulated MnPS<sub>3</sub>/Fe<sub>3</sub>GeTe<sub>2</sub> sample (D3). Considering the mismatch in the thermal expansion coefficient between Fe<sub>3</sub>GeTe<sub>2</sub> and the Si/SiO<sub>2</sub> substrate, it's possible that roughness in the substrate can clamp the vdW FM Fe<sub>3</sub>GeTe<sub>2</sub> and induce a net non-zero stress in device D1 and D2. Remarkably, substrate clamping has no significant influence in the evolution of exchange bias, suggesting that the dynamic evolution of exchange bias depends solely on the thermal cycling induced modification of MnPS<sub>3</sub>/Fe<sub>3</sub>GeTe<sub>2</sub> interface registry.

## Structural characterizations of the materials and their heterostructures

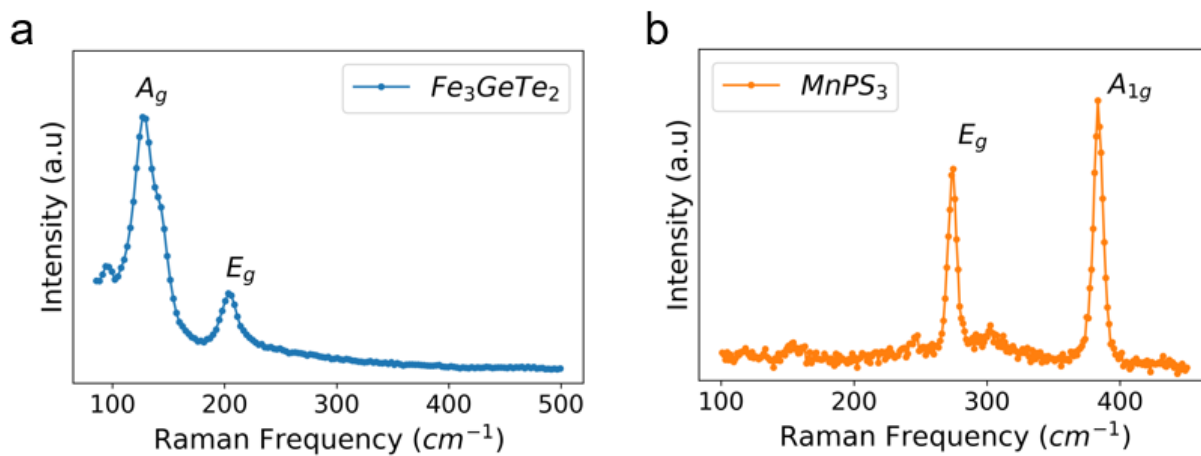


**Figure S4.** Raman spectroscopy of  $Fe_3GeTe_2$  and  $MnPS_3$  crystals used for fabricating devices in this work.

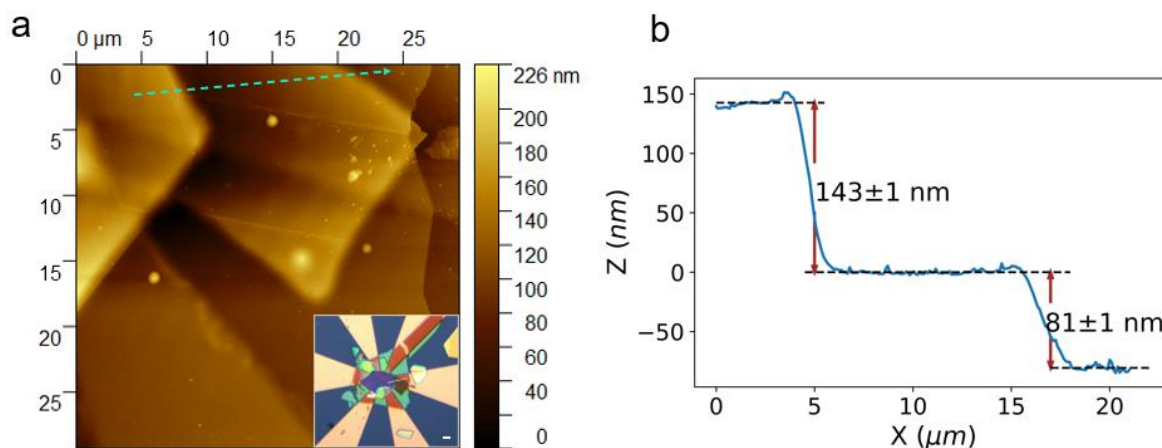


**Figure S5.** Atomic force microscopy (AFM) analysis for measuring the thickness of different layers in the vdW heterostructure D1. **a)** AFM image. The green dashed line shows the line used to calculate thickness. The inset shows an optical image of the sample. **b)** The linecut shows thickness of  $Fe_3GeTe_2$  layer to be close to 80 nm and  $MnPS_3$  flake to be close to 140 nm.

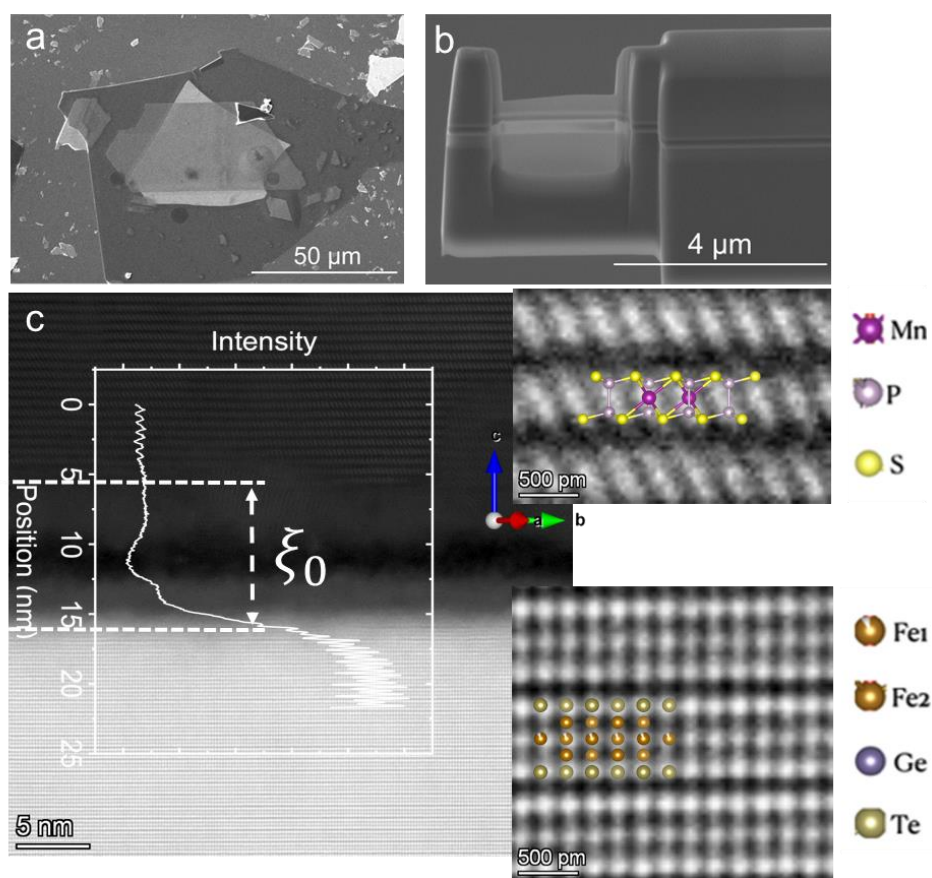


**Figure S6. Cross-sectional STEM sample preparation:** a) Scanning electron microscope image of h-BN/MnPS<sub>3</sub>/Fe<sub>3</sub>GeTe<sub>2</sub> stack, b) Cross-sectional lamella on a typical STEM grid, and c) Cross-sectional STEM of the stack with the inter-crystalline distance ( $\xi$ ) indicated. HAADF (high angle annular dark field) images of the crystalline regions are shown in the insets with colour-coded atomic positions.

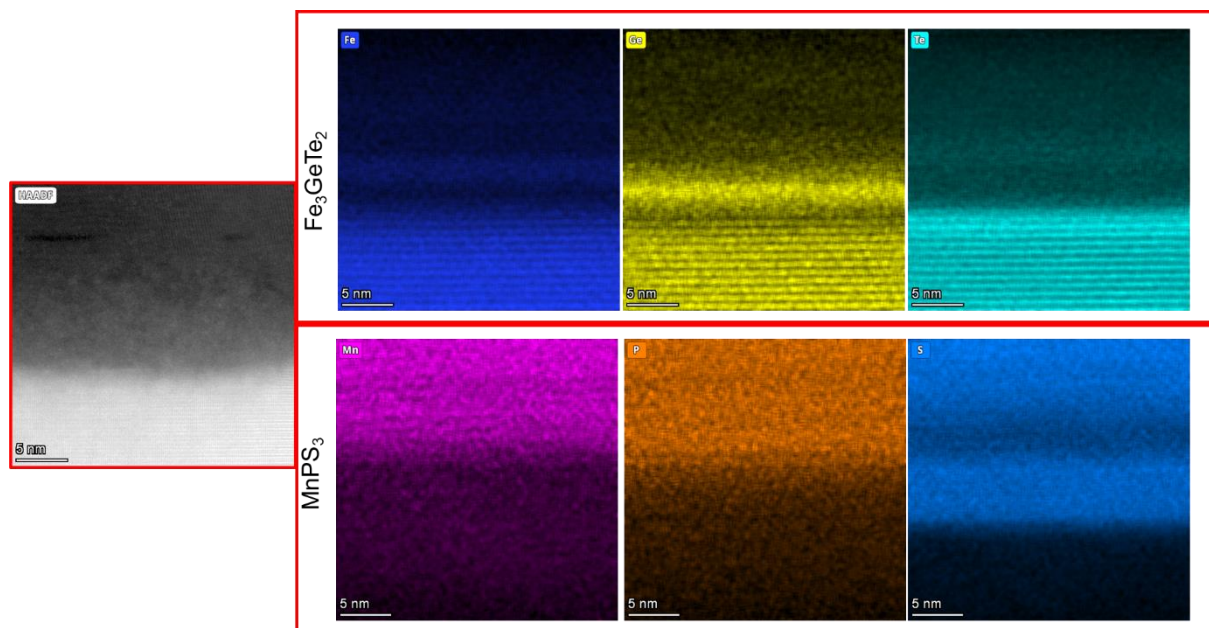


**Figure S7. Cross-sectional STEM EDX of the MnPS<sub>3</sub>/Fe<sub>3</sub>GeTe<sub>2</sub> interface:** Elemental mapping images acquired through STEM EDX reveal the migration of elements across the vdW gap. Particularly noteworthy is the translocation of sulfur from MnPS<sub>3</sub> layers proximate to the interface to the corresponding layers of Fe<sub>3</sub>GeTe<sub>2</sub>. This results in the formation of amorphous layers that act as a separator between the crystalline regions on either side of the vdW gap.

### Theoretical Calculations

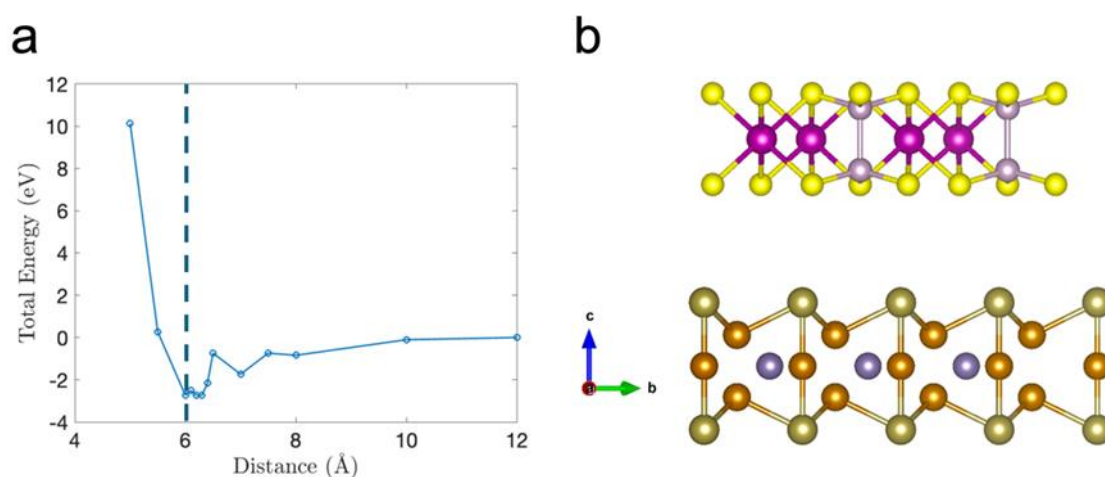


**Figure S8. Total energy dependence from first principles calculation of the interface between Fe<sub>3</sub>GeTe<sub>2</sub> and MnPS<sub>3</sub>:** First principles calculations using the Density Functional

Theory code VASP were performed for different vdW distances of  $\text{Fe}_3\text{GeTe}_2$  and  $\text{MnPS}_3$ . (a) shows the total energy which becomes unstable below 6 angstroms. (b) shows the  $\text{Fe}_3\text{GeTe}_2$  and  $\text{MnPS}_3$  stack used in the calculations.